Electrochimica Acta 448 (2023) 142168

Contents lists available at ScienceDirect

Electrochimica Acta

journal homepage: www.journals.elsevier.com/electrochimica-acta

Single walled carbon nanotube functionalisation in printed supercapacitor devices and shielding effect of Tin(II) Oxide

Seán Ryan [a,b,*], Michelle P. Browne [a,b,e], Ainur Zhussupbekova [a,b,c], Dahnan Spurling [a,b], Lorcan McKeown [a,b], Danielle Douglas-Henry [a,d], Lucy Prendeville [a,c], Sebastien Vaesen [a,b], Wolfgang Schmitt [a,b], Igor Shvets [a,c], Valeria Nicolosi [a,b,*]

[a] Centre for Research on Adaptive Nanostructures and Nanodevices (CRANN) and Advanced Materials and Bioengineering Research (AMBER), Trinity College Dublin, Dublin 2, Ireland
[b] School of Chemistry, Trinity College Dublin, Dublin 2, Ireland
[c] School of Physics, Trinity College Dublin, Dublin 2, Ireland
[d] Advanced Microscopy Laboratory (AML), Centre for Research on Adaptive Nanostructures and Nanodevices (CRANN) and Advanced Materials and Bioengineering Research (AMBER), Trinity College Dublin, Dublin 2, Ireland
[e] Helmholtz-Zentrum Berlin für Materialien und Energie, 14109 Berlin, Germany

ARTICLE INFO

Keywords:
Single walled carbon nanotubes
Supercapacitor
Anodic functionalisation
Tin(II) oxide
Asymmetric device
MXene

ABSTRACT

Due to this generation facing the biggest energy crisis of its lifetime, the spotlight has been shone more than ever on the rapid development of green energy and its storage. Supercapacitors are an integral technology in this renewable energy storage due to their high-power density. For an increased energy density however, one must expand the voltage window of the device and utilise electrolytes that allow for the maximum storage capability of the material. Single walled carbon nanotubes (SWCNT) were identified at the turn of the century as an excellent material for use in supercapacitor electrodes, however, at anodic potentials in sulphate-based electrolytes, they undergo irreversible oxidation which damage their electrical properties and affects long term cycling stability. Herein we provide an effective strategy to expand the voltage window of SWCNTs to 1.4 V in sulphate-based electrolytes through the small addition of tin (II) oxide (SnO), with a capacity of 102 F g^{-1} / 143 C g^{-1} at a current density of 2 A g^{-1}. We study the effect of SnO and propose a pseudo-reversible oxidation reaction in which the SWCNTs are protected from oxidation through the formation of Sn_3O_4. Finally, an asymmetric device using MXene is assembled to illustrate the advantage of the expanded voltage window on energy density and cycling stability, with a capacity retention of 90% after 7,500 cycles at 10 A g^{-1}.

1. Introduction

Since their discovery by Iijima [1] in 1991, carbon nanotubes (CNTs) have been at the forefront of advancements in materials science and nanotechnology. Single walled carbon nanotubes (SWCNTs) are particularly suited to energy storage applications due to their outstanding mechanical and electrical properties. SWCNTs have excellent electrical properties, with a carrier mobility of ~ 10,000 cm^2 V^{-1} s^{-1}, a room temperature conductivity in excess of 5 x 10^5 S m^{-1} and the capability to carry an electrical current density of ~ 4 x 10^9 A cm^{-2} [2–4]. SWCNTs also display exceptional mechanical properties with a Young's modulus of ~ 0.64 TPa and a tensile strength of ~ 37 GPa [5,6]. Due to these properties, SWCNTs are extremely well suited to energy storage applications, and in particular supercapacitor (SC) devices. The large capacitances obtainable from SWCNTs are due to their highly accessible surface areas in which most of the charge is stored in the electric double layer (EDL). However, electrochemically active functionalities on the terminals of the tubes also lead to a pseudocapacitive charge storage mechanism [7]. Further addition of redox-active functional groups although leading to an increase in the specific capacitance, leads to a decrease in conductivity and cycling stability [8].

Sulphate based electrolytes such as sulphuric acid or potassium sulphate are amongst the most widely used electrolytes in supercapacitor devices due to the large specific capacitances associated as a result of the small cationic radii [9]. In particular the H^+ ion possesses the highest specific capacitance due to the small hydration sphere

* Corresponding authors.
E-mail addresses: ryans46@tcd.ie (S. Ryan), nicolov@tcd.ie (V. Nicolosi).

https://doi.org/10.1016/j.electacta.2023.142168
Received 7 November 2022; Received in revised form 28 December 2022; Accepted 4 March 2023
Available online 5 March 2023

radius, a large ionic mobility and the highest molar ionic conductivity. To maximise the energy storage capacity of the next generation of supercapacitors an increase in the workable voltage window of the device is an attractive solution, in addition to using an electrolyte which maximises capacity, whilst maintaining the stability of the active material. The energy stored in an SC device is proportional to the voltage window squared.

The anodic functionalisation of SWCNTs was reported at the turn of the century by Sumanasekera et al. [10], with further studies expanding on the mechanisms at play carried out subsequently [11,12]. However, to our knowledge, no one to this point has presented an effective strategy to offset the anodic functionalisation of SWCNTs which in doing so expands the voltage window of a SWCNT-based supercapacitor device and maintains the integrity of the structure for enhanced cycling stability.

Tin(II) Oxide (SnO) is a p-type semiconductor [13] with a lead(II) oxide (PbO)-type layered tetragonal structure (P4/*nmm*). It is found naturally as the mineral romarchite and is environmentally friendly. The stability of the distorted layered structure is due to the coupling of the unfilled Sn(5p) with the antibonding combination arising from the interaction of the Sn(5s) and O(2p), with the resulting layered structure having a sizeable interlayer spacing of 4.85 Å [41]. This large interlayer gap and both the conversion and alloying reactions obtainable with lithium and sodium have led to SnO being recognised as a potential anode for future lithium/sodium-ion technologies. To date, most work has focused on the Tin(IV) Oxide in supercapacitor devices forming composites with reduced graphene oxide[14–16], or forming alloys with nickle foam [17,18]. Recently, work has been carried out with SnO [19]. However, to achieve reasonable capacitance, doping of SnO with manganese and the addition of potassium ferrocyanide to the electrolyte was required, which complicates the synthesis and increases the cost. One would assume that due to this layered nature, SnO would be suitable for intercalation pseudocapacitance, and this mechanism was investigated.

Herein we show that by combining SWCNT with a low mass loading of SnO, the anodic oxidation of the SWCNTs is inhibited as a quasi-reversible reaction instead takes place with the SnO allowing the workable voltage window to be expanded. The SWCNT/SnO composite is processed as an ink to allow it to be processed into SC devices using 3D extrusion printing, and an asymmetric device is assembled with a wide voltage window using MXene as the counter electrode material.

2. Material and methods

2.1. Synthesis of SnO

$SnCl_2$ (7.584 g, 0.04 mol, anhydrous, 98%, Alfa Aesar) was dissolved in ice-cold distilled water (400 ml) and placed on a magnetic stirring plate. NH_4OH (12.8 ml, 0.08 mol, 25%, Merck) was added dropwise and left to stir for 1 hour. The solution was transferred to centrifuge tubes and separated in the centrifuge (Heraeus Multifuge x1 Centrifuge) at 5000 rpm for 5 min. The $Sn(OH)_2$ precipitates were washed with distilled water (twice) and ethanol (once) before being re-dispersed in 60 ml of 70% methanol in a 100 ml round-bottom flask and heated at 120 °C for 24 h under reflux. The product was again separated via centrifuge, repeating the wash procedure as above. The final product was kept in ethanol solution and dried as needed, to minimise the risk of oxidation to SnO_2.

2.2. Printing of devices

SnO inks were formed using Tuball SWCNTs (0.2%) dispersed in carboxymethyl cellulose (CMC - 0.3%) and H2O. The ratio of SWCNT to SnO was 9:1. In this work the various SnO inks were printed with a Nano3DPrint extrusion printer, without the need of additives to aid printing. For these prints, the material was extruded using a 0.26 mm internal diameter nozzle onto weighed and cleaned glass slides. The material was extruded onto a print bed set to 60 °C to aid the drying of the printed patterns. The print speed was held at 200 mm/min to maintain consistent line and pattern formation and so adjustments could be made easily during the print process. As standard, three printed passes were deposited and allowed to dry in each print run to provide a complete homogenous film before further layers were deposited. The patterns used were designed using AutoCAD (Autodesk Inc,) and the final print path GCode was generated using the Simply3D slicing software to provide x y z pathing for the designed patterns. Successive layers were printed at 90° to one another to eliminate issues that could potentially arise from print defects.

Printed devices were placed in a tube furnace and heated under vacuum with an argon air flow at a ramp of 10 °C/min with a 2 hour hold at 400 °C to remove H_2O and carbonise the CMC binder. Silver contacts and a protective resin layer were added subsequently.

MXenes were produced as done by Borghetti et al. [20], and printed using the same parameters as the SWCNT/SnO electrodes. Briefly, Ti_3AlC_2 MAX phase powder (1 g, Carbon-Ukraine ltd.) was delaminated using 9 M HCl (20 mL, Sigma) and LiF powder (1.6 g, Sigma) in a PTFE vessel. The solution was left stirring at 400 rpm at 35 °C for 24 h to obtain etched, multilayer $Ti_3C_2T_x$ MXene. The delaminated MXenes were obtained through washing with deionized water and centrifugation at 5000 rpm using a Thermo Scientific Heraeus Multifuge X1 for 5 min, discarding the supernatant and repeating several times, until the pH of the supernatant had reached at least 6. The dispersion was then centrifuged at 1500 rpm for 30 min to sediment any multi-layer MXene or unreacted MAX phase.

2.3. Electrochemical analysis

A three-electrode electrolytic cell was formed for electrochemical testing using a working electrode, an Ag/AgCl double junction electrode as reference electrode, and a graphite rod as a counter electrode. Two electrode cells were formed using SWCNT/SnO as the positive electrode and MXene as the negative electrode. All electrochemical measurements: such as cyclic voltammetry (CV), galvanostatic charge-discharge (GCD) and electrochemical impedance spectroscopy (EIS) were performed using a Bio Logic VMP 300 and analysed using the EC-Lab software. CVs were recorded at scan rates of 5, 10, 20, 50, 100, 200, 500, 1000, 2000 mV s^{-1} from −0.4 to 1 V (vs Ag/AgCl) in H_2SO_4 and −0.2 to 1 V (vs Ag/AgCl) in K_2SO_4. GCD measurements were ran using the same voltage windows as for the CVs at rates of 1, 2, 5 and 10 A g^{-1}. EIS was recorded at an open circuit potential from 1000 kHz to 10 mHz. The electrode was left at an open circuit voltage for 1 hour to stabilise prior to measurements and ensure no faradaic charge transfer processes were occurring. Upon commencement of the readings the voltage remained steady throughout. The Z-fit software from EC-lab was used to fit equivalent Randle's circuits to EIS spectra and obtain values for the components.

2.4. Characterization techniques

Scanning Electron Microscopy (SEM) was carried out using the Zeiss ULTRA plus Gemini SEM microscope in high vacuum mode with an acceleration voltage of 5 keV, a working distance of 6 mm and a 30 μm aperture located in the Advanced Microscopy Laboratory (AML) of TCD. Images were recorded using both the InLens detector.

Structural characterisation of the CNTs was done by Transmission Electron Microscopy (TEM). This was performed using a FEI Titan 80–300 Thermo Fisher Scientific, fitted with a Schottky field emission gun. The operating voltage was set to 300 kV and images were recorded using a Gatan UltraScan CCD camera. Images of the CNTs were recorded in overfocussed conditions to enhance the phase contrast. Elemental composition was determined by Energy Dispersive X-Ray Spectroscopy (EDS) using a Bruker XFlash 6–30 EDS detector. Elemental mapping regions were imaged in Scanning Transmission Electron Microscopy

(STEM) mode with an angle annular dark-field (HAADF) detector. EDS spectrum analysis was done using Bruker Esprit 2.0.

X-ray diffraction (XRD) measurements were performed using a Panalytical X'Pert Pro-diffractometer with a Cu Kα source (λ=1.5406 nm). Symmetric scans were run over a 2θ range of 10 to 75°, with a step size of 0.0084°

Raman measurements were performed using a Horiba Raman system (LabRAM ARAMIS HORIBA Jobin Yvon) with integrated LabSpec 5 software. The objective lens was 100x (0.90 NA) and the laser wavelength was 524 nm. Spectra were recorded by defining a 10 μm x 10 μm area with a step size of 5 μm with an integration time of 2 s used for each scan.

Fourier transform infrared (FTIR) spectra were recorded on a PerkinElmer Spectrum 100 equipped with a universal total reflectance (Diamond/KRS-5 sandwich assembly) sampling accessory. The spectra were recorded from 4000 to 350 cm^{-1}.

X-Ray Photoelectron Spectroscopy (XPS) spectra were recorded using an Omicron MultiProbe XPS instrument. High resolution spectra were obtained at a 50 eV pass energy with a monochromatic Al Kα (XM 1000, 1486.6 eV) source. Films were attached to stainless steel sample holder by copper tape and degassed in the load lock and preparation chamber prior to the measurement. Obtained spectra were analysed in the CasaXPS software with Gaussian-Lorentzian shape fitting and Shirley background.

To assess the surface area of the samples, nitrogen adsorption at 77 K were measured using a Quantachrome Autosorb-IQ. Prior to the measurements, each sample (+/- 200 mg) has been activated overnight at 150 °C under secondary vacuum. In a typical experiment, adsorption curves have been measured in the range of 0.0001 – 0.99 *p/p0*, and desorption curves in the range of 0.99 – 0.3 *p/p0*. To determine the surface area, we used the classic Brunauer-Emmett-Teller (BET) method [21]. This method consists of the linearisation of the isotherm into a "BET plot" which allows the determination of the nitrogen monolayer adsorption capacity of the samples. Knowing the cross-sectional surface of adsorbed N_2 molecules (0.162 nm^2), we can determine the BET surface area of the sample.

3. Results and discussion

SWCNT/SnO composite electrodes were produced using extrusion printing as shown in Fig. 1A and B and were tested as SC devices in a three electrode wet electrochemical cell setup using CV (cyclic voltammetry), GCD (galvanostatic charge-discharge) and EIS (electrochemical impedance spectroscopy) measurements. The effect of the presence of SnO on the functionalisation of the SWCNTs was subsequently characterised.

3.1. Materials characterization

Raman spectroscopy is a powerful technique for probing the structure of graphitic materials and in particular CNTs. Five distinctive Raman bands from SWCNTs are shown in Fig. 2A and B: the radial breathing mode (RBM) at the low frequency end (~ 100 – 200 cm^{-1}), the D-band (1329 cm^{-1}), the G-band (1577 cm^{-1}) which contains both the G^+ and G^- band, the M-band [22] (1730 cm^{-1}) and the G' band (~2650 cm^{-1}). When SWCNTs are functionalised, the hybridization of the carbon is changed from sp^2 to sp^3 [23]. The D-band (A_{1g} symmetry) represents forbidden out of plane vibrations [24] in a perfect graphite lattice and is a key indicator of deviations from the ideal structure, whilst the G-band (E_{2g} symmetry) is due to in-plane vibrations and characteristic of sp^2 hybridized carbon; thus the ratio of the D/G band intensities (I_D/I_G) allows one to quantify disorder in the SWCNT structure and deviations from the perfect sp^2 network [25,26]. The I_D/I_G ratio for both the pristine and annealed SWCNT electrodes remain constant at 0.04 respectively, whilst for the SWCNT electrode subject to use in H_2SO_4 the ratio increases to 0.07 (Fig. 2A). In comparison, all the SWCNT/SnO composite electrode's I_D/I_G ratio remain constant at 0.03 (Fig. 2B), suggesting that electrochemical oxidation is being inhibited by the presence of SnO, which again agrees with the electrochemical data.

FTIR was carried out on 5 samples in Fig. 2C (Pristine SWCNTs, Annealed SWCNTs, Annealed SWCNT/SnO composite, H_2SO_4 SWCNT/SnO composite, H_2SO_4 SWCNTs). The H_2SO_4 SWCNT sample displays a peak at 1720 cm^{-1} which is due to the stretching of the carbonyl group (C═O)[27–29] and is unique to this spectrum. The band at 1250 cm^{-1} is partly due to C—O stretching vibration [27,30] and is further confirmation of the oxidative process. In addition, the S═O symmetric (1150 cm^{-1}) and asymmetric vibrations (1300 cm^{-1}) lie in this region leading to the broad absorption band [31]. The long broad peak at 3350 cm^{-1} is due to the O—H stretch [32]. The peak at 890 cm^{-1} may be due to S—OR bond [33], but lies in the fingerprint region so may be hard to

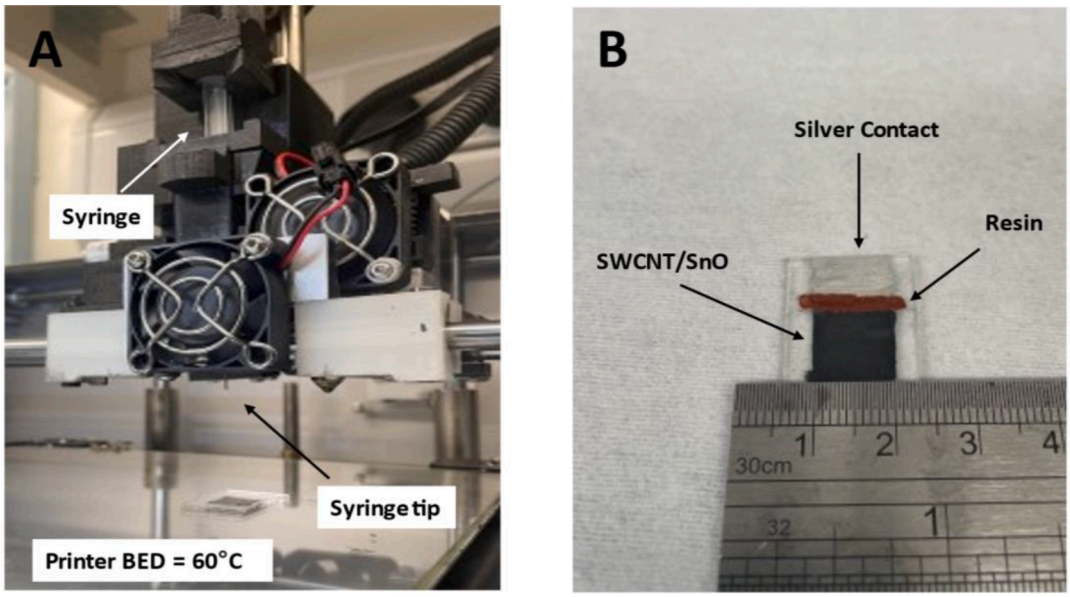

Fig. 1. (A) Picture of Nano3DPrint extrusion printer used to fabricate SC devices (B) Picture of an as fabricated SC device with a silver contact and a protective resin layer.

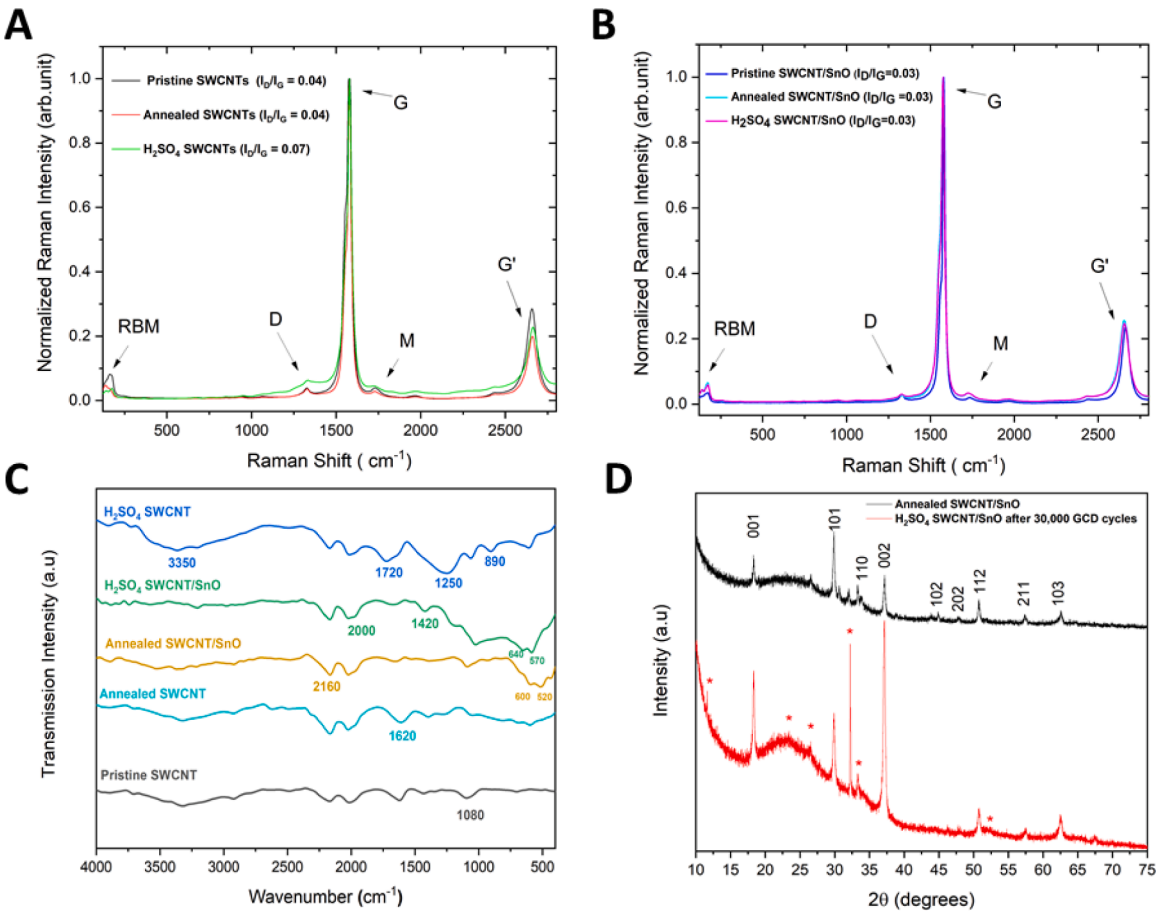

Fig. 2. Material characterisation of SWCNTs and SWCNT/SnO. Raman spectroscopy for (A) pure SWCNT SC devices and (B) SWCNT/SnO SC devices. (C) FTIR of pristine SWCNT (grey), annealed SWCNT (cyan), annealed SWCNT/SnO (yellow), SWCNT/SnO post-mortem use in H_2SO_4 (green) and SWCNT post-mortem use in H_2SO_4 (blue). (D) X-ray diffraction pattern of SnO/SWCNT pre/post-mortem use after 30,000 GCD cycles in H_2SO_4 (a y-offset has been applied on the relative intensities for display purposes). .

distinguish. C═C [27,30] stretching at 1620 cm^{-1} is common to all samples, although more pronounced in the pure CNT samples as expected. The peak at 1080 cm^{-1} is due to C—O [29,34], and this occurs on the tails of the CNTs and is common to all samples. Peaks at 2160 and 2000 cm^{-1} are seen in all samples and are consistent with overtones of the 6 ringed carbon of the graphene/graphite structure of the CNTs [35–37]. The peaks on the spectrums obtained from the samples with SnO at 640, 600, 570 and 500 cm^{-1} are due to the Sn-O vibrations [19, 38–40].

The structure of the SWCNT/SnO composites were analysed using XRD pre- and post-mortem in SC devices in Fig. 2D. The annealed SWCNT/SnO is consistent in structure with that of pure SnO (JCPDS 06–0395) [41]. This confirmed that the thermal carbonisation of the CMC binder did not cause the SnO to oxidise to SnO_2, consistent with previous reports on the thermal stability of SnO [13]. Post cycling, additional XRD peaks (*) are recorded consistent with Sn_3O_4 (JCPDS 16–0737). Therefore, it is suggested that a hybrid structure exists where both SnO and Sn_3O_4 exist in tandem.

3.2. XPS

X-Ray Photoelectron Spectroscopy (XPS) was utilised in this study to determine the changes (if any) to the SWCNTs after H_2SO_4 treatment when the SWCNTs were mixed with/without SnO. In order to compare the various samples, first the high resolution C1s region was analysed, Fig. 3A- D.

The C1s region of the SWCNT annealed sample was fitted with typical contributions of annealed SWCNTs i.e. presence of C—C sp^3 due to C—O and carbonyl contributions in the C—C sp^2 structure due to the annealing process, Fig. 3A [42,43]. After H_2SO_4 treatment, the sample appeared to have further oxidised due to the decrease in the C—C sp^2 peak and the disappearance of the π-π* bonds which shows a decrease in the graphitic carbon in the sample, Fig. 3B. This is in agreement with the reported Raman results. Furthermore, the C—C sp^3 contribution increases, indicating the introduction of defects to the carbon structure, Table 1. These defects can be easily explained by the appearance of the carboxylic group contribution (O═C—OH) after H_2SO_4 treatment.

Interestingly, for the SWCNT annealed sample with the SnO, the fitted contributions before and after H_2SO_4 treatment were not altered, Fig. 3C and D. This result indicates that the SnO hinders the SWCNTs from oxidation during the H_2SO_4 process. Additionally, when comparing the pure SWCNT annealed sample, Fig. 3A, to the SWCNT/SnO annealed sample, Fig. 3C, it is evident that the SnO doesn't form bonds with the SWCNTs as the two samples exhibit near identical fits. However, from the high resolution $Sn3d_{5/2}$ region, Fig. 3E, the shift in the peak to a higher binding energy by 0.2 eV indicates that the original SnO is itself oxidised after the H_2SO_4 treatment in agreement with the XRD analysis. Hence, the SnO may block/shield the SWCNT from being oxidised as it itself is interacts with the anions present, resulting in partial oxidation during cycling with H_2SO_4.

3.3. Electron microscopy

Scanning electron microscopy (SEM) analysis was carried out to

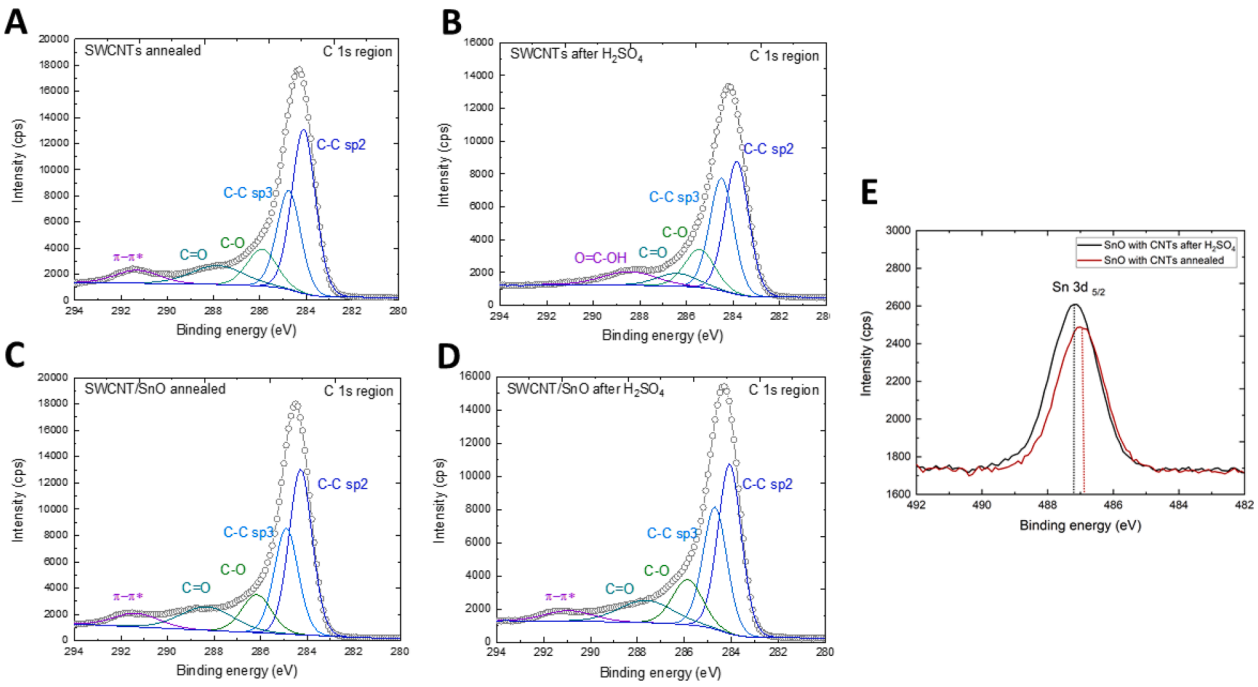

Fig. 3. (a) XPS C1s core level for SWCNT annealed. (b) XPS C1s core level for SWCNT post use in SC device with 0.5 M H_2SO_4. (c) XPS C1s core level for SWCNT/SnO annealed. (d) XPS C1s core level for SWCNT/SnO post use in SC device with 0.5 M H_2SO_4 (e) XPS Sn $3d_{5/2}$ region of SWCNT/SnO post use in SC device with 0.5 M H_2SO_4 and SWCNT/SnO annealed.

Table 1
XPS C1s contributions and corresponding binding energies for SWCNT and SnO/SWCNT electrodes .

C1s Contribution	SWCNTs Annealed	SWCNTs post H_2SO_4	SWCNTs/SnO Annealed	SWCNTs/SnO post H_2SO_4
sp2	43.8% 284.1 eV	38.5% 283.8 eV	40.9% 284.2 eV	39.9% 284 eV
sp3	26.3% 284.8 eV	32.5% 284.5 eV	27% 284.9 eV	29.5% 284.7 eV
C–O	12.3% 285.9 eV	13.8% 285.4 eV	12.1% 286.2 eV	13.6% 285.9 eV
C═O	11.2% 287.8 eV	6.3% 286.4 eV	13.4% 288.3 eV	12% 287.6 eV
C═O – OH	n/a	8.9% 288.4 eV	n/a	n/a
π-π*	6.4% 293.1 eV	n/a	6.6% 291.3 eV	5% 290.9 eV

examine the morphology of the SWCNTs and SnO both pre and post use in SC devices. There was no noticeable difference in morphology between the pure SWCNT SC devices pre/post use due to the limitations of the resolution of the SEM, Fig. 4A and B. The morphology of the SnO however does exhibit differences once it has undergone use in SC devices. Pristine SnO has a relatively clear surface on the square platelet, Fig. 4C and D. However, upon cycling this platelet becomes covered in nanoparticles, Fig. 4E and F. Using the XRD analysis it may be assumed these nanoparticles consist of Sn_3O_4, and due to their reversible production, the SWCNTs are shielded from undergoing any irreversible oxidation processes in the electrolyte.

Transmission electron microscopy (TEM) was utilised to characterise the morphology of the tubes of the SWCNTs having undergone the various treatments (Fig. 5). Both as received (Fig. 5A) and annealed SWCNTs (Fig. 5B) have a very similar appearance overall with subtle differences. The walls of the annealed SWCNT appear less clear and rough due to the carbonisation of the CMC, whilst in addition the tubes have a greater tendency to clump together. The tendency of annealed samples to clump together is due to the removal of the CMC which acts as a repellent between adjacent tubes, and thus its removal would lead to favourable conditions for bundle formation [43].

Pure SWCNTs analysed post use in devices displayed further deterioration in the wall clarity (Fig. 5C), agreeing with the suggestion of functionalisation and wall damage to the graphitic structure of pure SWCNTs. In addition, nanoparticles were distributed on the walls of the SWCNT matrices (Fig. 5D), which were identified as sulphates originating from the electrolyte using EDX (Fig. 5E and Supplemental Figure 1A) and consistent with the presence of sulphur in the XPS survey scan (Supplemental Figure 1C). SWCNTs from the composite with SnO similarly displayed clumped morphologies with small particles distributed throughout (Fig. 5F and G) identified as SnO with trace amounts of sulphur using EDX and consistent with the XPS survey scan (Fig. 5H, Supplemental Figure 1B and D).

3.4. Mechanism – electrochemical anodic oxidation and SnO

The mechanism for the anodic oxidation and subsequent functionalisation of SWCNTs was first described by Sumanasekera et al. [10]. Initial contact between H_2SO_4 and SWCNTs with no external potential applied leads to a spontaneous chemical reaction in which the SWCNT walls are decorated with H_2SO_4 molecules and HSO_4^- ions according to Eqs. (1) and (2). This spontaneous reaction is unique to CNTs and does not take place in graphite [10,44,45]. This leads the cell potential to climb to roughly 0.2 V vs Ag/AgCl reference as was observed experimentally under open circuit prior to electrochemical testing and is in agreement with Ref [10] and Ref [44].

$$e^- + H_2SO_4 \rightarrow 1/2H_2 + HSO_4^- \ (cathode) \quad (1)$$

$$SWCNT^+HSO_4^- + vH_2SO_4 \rightarrow SWCNT^+HSO_4^- \cdot vH_2SO_4 + e^- (anode) \quad (2)$$

Upon the commencement of cyclic voltammetry/galvanostatic charging and increasing the potential from ~0.2 V to 0.5 V vs Ag/AgCl, 'overcharging' is observed in which the cell potential causes the neutral H_2SO_4 molecules in the interstitial channels of the tube bundles to be

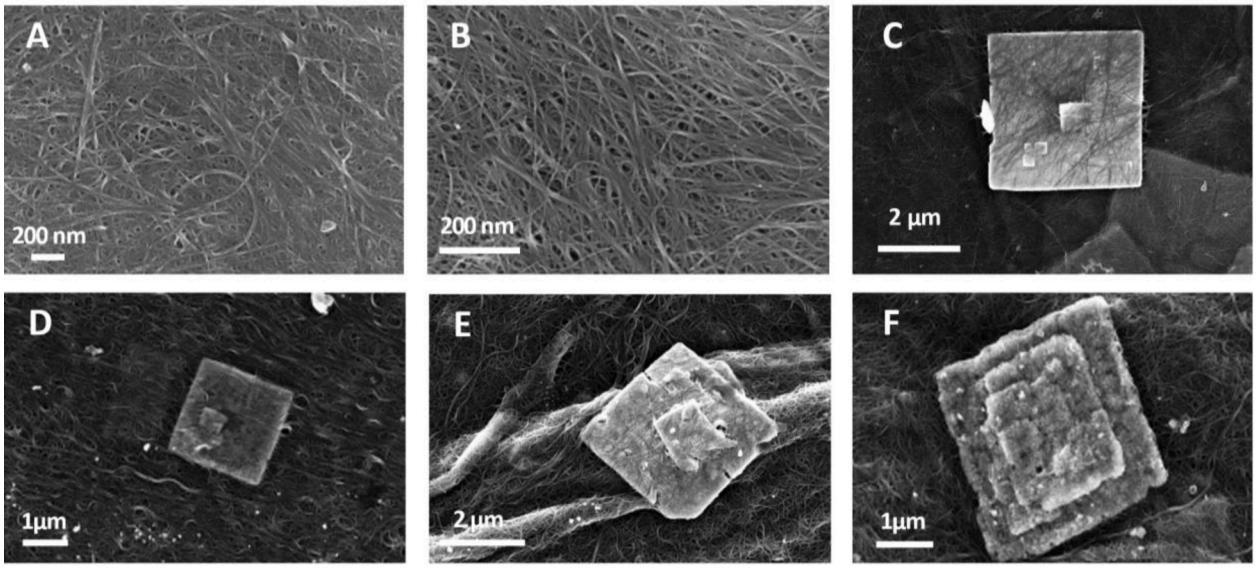

Fig. 4. SEM images of (A) annealed SWCNTs, (B) SWCNTs post use in 0.5 M H_2SO_4, (C – D) annealed SWCNT/SnO, (E – F) SWCNTs/SnO post use in 0.5 M H_2SO_4. .

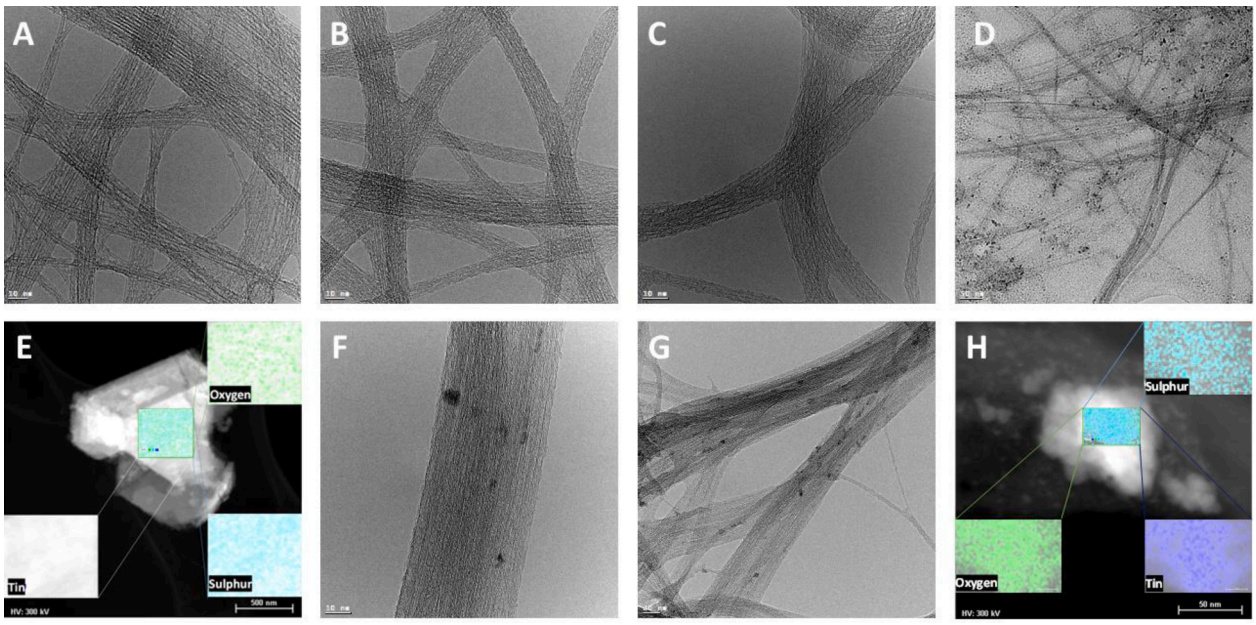

Fig. 5. TEM images of (A) as received SWCNT material, (B) annealed SWCNT sample, (C) annealed SWCNT sample post use in supercapacitor device in H_2SO_4 (D) and particles dispersed throughout after use, (E) EDX map of particles dispersed on SWCNT post use in H_2SO_4, (F) annealed SWCNT/SnO sample post use in 0.5 M H_2SO_4 (G) and associated particles throughout, (H) EDX map of particles dispersed on SWCNT/SnO tubes post use in H_2SO_4.

converted to HSO_4^- and hydrogen is evolved and lost as shown in Eqs. (3) and (4) [10–12,45,46]. This conversion of H_2SO_4 creates new holes in the SWCNT π-band which is consistent with the XPS (Fig. 3B) and Raman (Fig. 2A) results measured.

$$SWCNT^{+}HSO_4^{-}\cdot\upsilon H_2SO_4 \rightarrow SWCNT^{(1+\delta)+}\left(HSO_4^{-}\right)_{(1+\delta)}\cdot(\upsilon-\delta)H_2SO_4 + \delta e^{-} + \delta H^{+}\ (anode) \quad (3)$$

$$\delta H^{+} + \delta e^{-} \rightarrow \delta/2H_2\ (cathode) \quad (4)$$

As the potential exceeds 0.5 V vs Ag/AgCl, 'overoxidation' occurs in which the presence of H_2O allows for the irreversible electrochemical formation of C—O bonds, leading to further functionalisation of the SWCNTs with a disordered structure containing C, H and O [47], aligning again with the observations from XPS and FTIR.

Evidence shows that SnO inhibits the formation of holes in the sp^2 SWCNT structure and the subsequent irreversible electrochemical formation of C—O bonds, through itself pseudo-reversibly reacting with the available HSO_4^-, forming Sn_3O_4 in the process. Through this, the SWCNT is protected from 'overoxidation' and thus maintains the integrity of the tube and the electrochemical performance associated.

3.5. Electrochemical analysis

The functionalisation of pure SWCNTs in the presence of H_2SO_4 and K_2SO_4 was shown by the initial CV response at 5 mV s^{-1}. As shown in Fig. 6B and D, between the initial and 10th cycle drastic changes have occurred to the rectangular shape of the voltagramms of the pure SWCNTs with further changes occurring with subsequent cycles. These

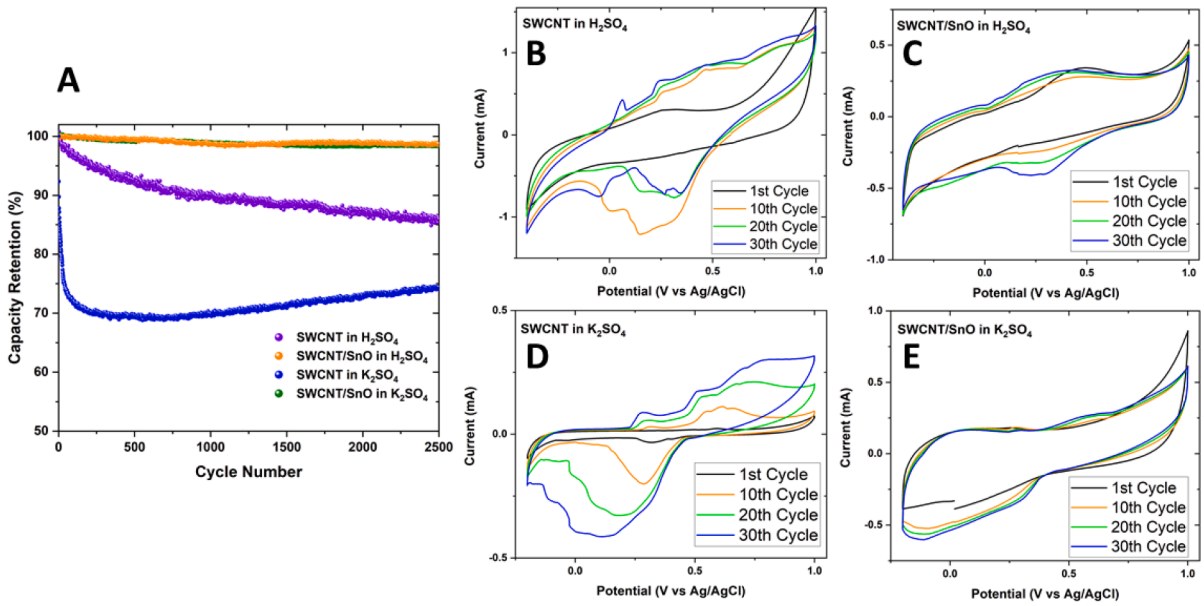

Fig. 6. (A) Capacity retention at 10 A g^{-1} of various SC devices over 2,500 cycles. (B) CV at 5 mV s^{-1} of SWCNT H_2SO_4. (C) CV at 5 mV s^{-1} of SWCNT/SnO H_2SO_4. (D) CV at 5 mV s^{-1} of SWCNT K_2SO_4. (E) CV at 5 mV s^{-1} of SWCNT/SnO H_2SO_4.

changes are seen by the additional wide redox peaks on the cathodic sweep at roughly 0.25 V in H_2SO_4 and 0.1 V in K_2SO_4 and on the anodic sweep at 0.25 V, 0.5 V and 0.75 V for K_2SO_4 whilst in H_2SO_4 there is no distinctive peak, just a broad region from 0 – 1 V in which the redox processes are taking place.

Conversely, as shown in Fig. 6C and E, a 10% mass fraction of SnO prevents this functionalisation from occurring, with subsequent cycles appearing almost identical to previous ones (the increase in the overall area is due to additional electrode wetting with subsequent cycling). The observable broad reaction peaks that deviate from the typical rectangular shape associated with EDL capacitance (EDLC) are related to the redox processes due to surface oxygen groups on the terminals of the tubes [23,48].

The advantage of inhibiting the functionalisation is apparent in the cycling stability data shown in Fig. 6A. With functionalisation, the charge capacity of the SWCNTs falls to 85% in H_2SO_4 and 74% in K_2SO_4 of its initial value after 2,500 cycles. Through the use of SnO to inhibit the functionalisation, after 2,500 cycles, capacity retention remains at 99%. To further demonstrate the effectiveness of SnO/Sn_3O_4 at preventing the functionalisation of SWCNTs, extended cycling for 15,000 and 30,000 cycles was recorded with the resulting CVs (Supplemental Fig. 2A) displaying only minor alterations and the capacity retention remaining in excess of 95% (Supplemental Fig. 2B) whilst both SnO/Sn_3O_4 were still present (Fig. 2D). Herein we define capacity retention as the ratio of the capacitance at a given cycle to the value measured during the initial cycle. The over-oxidation necessary for functionalisation leads to defects and degradation of the polymer structure of the tube, and this causes a decline in performance. EIS was carried out on both pure SWCNT and SnO/SWCNT in both electrolytes (Supplemental Fig. 3). The EIS fitting of the equivalent circuit showed all electrodes displayed similar performances in terms of charge transfer resistance both pre/post use, with the electrodes with SnO having slightly higher resistances due to the presence of the non-conductive oxide (Supplemental Fig. 3 and Supplemental Table 1).

Functionalisation leads to greater charge storage at low scan rates, however, as shown in Table 2, as the scan rate increases, the gap between the charge capacity levels off, as these surface redox reactions do not have time to take place. As the CVs of the functionalised SWCNTs differ significantly in shape from the SWCNT/SnO composite it is more correct and representative of the electrode performance to compare in terms of Coulombs as the capacitance is not constant throughout the potential window, as shown in Table 2 (note that SWCNT/SnO are represented in Farads and Coulombs as they display rectangular CVs) [49]. For real world applications where supercapacitors are expected to act in an ultrafast fashion the SWCNT/SnO composite is favoured due to its enhanced cycling stability.

The electrochemistry of the SnO/SWCNT composite electrode in H_2SO_4 is shown with a CV plot at various scan rates and the GCD curve at various current densities (Fig. 7A and B). At 2 A g^{-1} which corresponds to a time roughly equivalent to a rate of 60C for a battery it delivers a capacitance of 102 F g^{-1} which would be a normal operating rate for a supercapacitor [50], whilst at 10 A g^{-1} it delivers 60 F g^{-1}. The specific capacitance (C_{sp}) was evaluated from CV curves using Eq. (5) and GCD curves using Eq. (6), where m is the mass of the electrode, υ is the scan rate, V_a and V_c are the anodic and cathodic cut-off potentials, and I is the current. As the CVs present are not perfectly rectangular, and the GCD curves not perfectly triangular displaying a linear time dependant change in potential at constant current [50] the integral forms are used

Table 2
Capacitance in F g^{-1} and C g^{-1} of various tested electrodes at various scan rates.

Scan Rate / Composite	5 mV s^{-1}	10 mV s^{-1}	20 mV s^{-1}	50 mV s^{-1}	100 mV s^{-1}	200 mV s^{-1}	500 mV s^{-1}	1000 mV s^{-1}	2000 mV s^{-1}
SWCNT H_2SO_4	288 C g^{-1}	223 C g^{-1}	174 C g^{-1}	128 C g^{-1}	100 C g^{-1}	78 C g^{-1}	53 C g^{-1}	39 C g^{-1}	27 C g^{-1}
SWCNT K_2SO_4	387 C g^{-1}	248 C g^{-1}	154 C g^{-1}	81 C g^{-1}	50 C g^{-1}	35 C g^{-1}	27 C g^{-1}	23 C g^{-1}	20 C g^{-1}
SWCNT/SnO H_2SO_4	171 F g^{-1}	128 F g^{-1}	96 F g^{-1}	73 F g^{-1}	62 F g^{-1}	55 F g^{-1}	47 F g^{-1}	39 F g^{-1}	28 F g^{-1}
	240 C g^{-1}	179 C g^{-1}	134 C g^{-1}	102 C g^{-1}	87 C g^{-1}	77 C g^{-1}	65 C g^{-1}	54 C g^{-1}	39 C g^{-1}
SWCNT/SnO K_2SO_4	88 F g^{-1}	77 F g^{-1}	54 F g^{-1}	41 F g^{-1}	36 F g^{-1}	33 F g^{-1}	27 F g^{-1}	23 F g^{-1}	18 F g^{-1}
	105 C g^{-1}	92 C g^{-1}	64 C g^{-1}	50 C g^{-1}	43 C g^{-1}	39 C g^{-1}	33 C g^{-1}	28 C g^{-1}	21 C g^{-1}

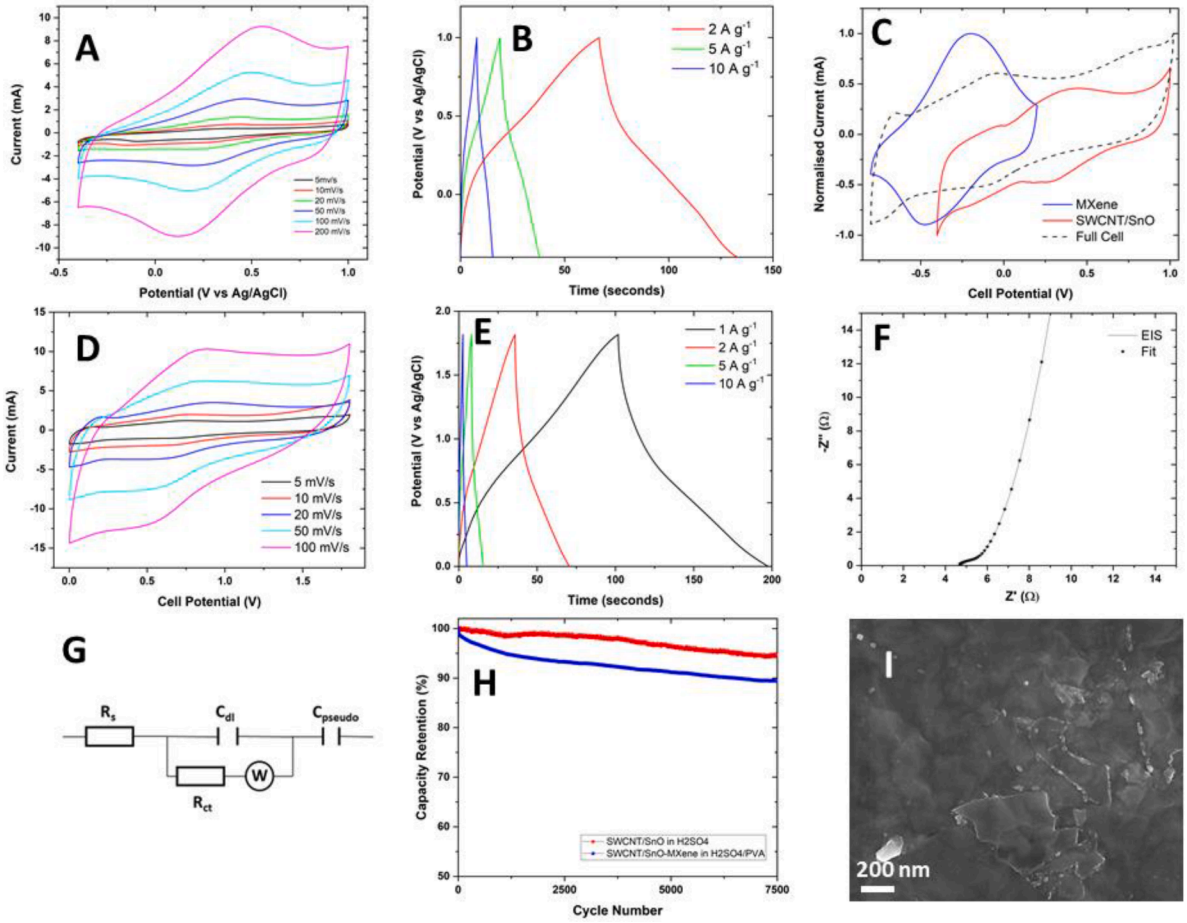

Fig. 7. (A) CV plot for SWCNT/SnO, (B)GCD curves at various rates for SWCNT/SnO, (C) CV plots of MXene, SWCNT/SnO and asymmetric full cell at 10 mV s^{-1}, (D) CV plot of asymmetric device at various scan rates, (E) GCD curve at various rates for asymmetric device, (F) EIS spectra of asymmetric device with Z-fit approximation overlayed, (G) equiavalent Randle's circuit used to represent supercapaciotr electrodes, (H) capacity retention of SWCNT/SnO in three electrode configuration and in asymmetric device over 7500 cycles, (I) SEM image of MXene electrode.

in Eqs. (5) and (6) to account for the non-ideality [51,52].

$$C_{sp} = \frac{1}{m\upsilon(V_a - V_c)} \int_{Vc}^{Va} I\,(V\,)dV \tag{5}$$

$$C_{sp} = \frac{I}{m} \int \frac{1}{V(t)} dt \tag{6}$$

In the voltage window tested the SnO has no capacitive effect except that which its surface area contributes to the EDLC, which is negligible when compared to the SWCNTs. This was demonstrated as by increasing the mass content of SnO from 10 to 50, 70 and 90%, there was a fall in capacitance owing to the replacement of the SWCNT with SnO (Supplemental Table 2). The specific surface area of SnO calculated from the N_2 isotherms (Supplemental Figure 4) using the classic BET method was 12.98 m^2 g^{-1} whilst the SWCNT specific area was 240.242 m^2 g^{-1}, thus the EDLC available is far greater through use of the SWCNT.

Due to its layered structure, it was thought SnO would partake in intercalation pseudocapacitance. The potential intercalation pseudocapacitance was investigated by exploring more negative potentials in the three-electrode setup. Upon repeated cycling, poor coulombic efficiency was recorded and diminishing currents for subsequent cycles as shown in Supplemental Figure 5. At these negative potentials, a reduction reaction happens in place of/in parallel to ion intercalation which reduces the SnO to metallic tin. During the subsequent anodic sweep not all of the metallic tin is re-oxidised to SnO resulting in the poor coulombic efficiency. This agrees with previous work carried out on Tin(II) Oxide sensors [53]. Therefore it is of no benefit to expand the voltage window to include this reaction as it is not fully reversible and the limit of the cathodic sweep was kept at −0.4 V vs Ag/AgCl reference.

To demonstrate the advantage of extending the voltage window to real world applications, an asymmetric device was assembled using MXene ($Ti_3C_2T_x$) as the negative electrode and 3 M H_2SO_4 in polyvinyl acetate (PVA) as the electrolyte. MXenes to date have shown great promise as high-rate electrodes for pseudocapacitive energy storage due to their highly reversible surface redox reactions [54], their 2D structure and the large accessible surface area available. As both electrodes present in this device display the same charge storage mechanisms (EDLC and pseudocapacitance) one may consider it an asymmetric device [49]. SEM images of the MXene sheets used are shown in Fig. 7I. With the MXene electrodes working range between −0.8 and 0.2 V vs Ag/AgCl (Supplemental Figure 6), the working voltage window of the device was set at 0 - 1.8 V (Fig. 7C, D and Supplemental Figure 7).

The maximum power of the asymmetric device was calculated using Eq. (7) [52,55,56], where $V_{charged}$ is the voltage of the device and ESR is the equivalent series resistance of the electrode:

$$P_{max} = \frac{V_{charged}^2}{4 \times ESR} \tag{7}$$

The ESR was calculated by using EIS and fitting the resulting Nyquist plot with an equivalent Randle's circuit as shown in Fig. 7G. R_s, the point of intersection of the real axis at high frequency is the internal/series resistance and includes the intrinsic electronic resistance of the electrode material, the ohmic resistance of the electrolyte and the interfacial

resistance between the electrode and current collector [55]. R_{ct} is the charge transfer resistance, C_{dl} is the double layer capacitance, and W is the Warburg element used to describe the impedance of diffusion of mobile charges in the electrode whilst C_{pseudo} is the pseudocapacitance obtainable in both the SWCNT [7,57] and MXene [58] electrodes.

The ESR is a sum of the internal resistance (4.62 Ω) and the charge transfer resistance (0.99 Ω). This leads to a maximum power density of 51.5 kW kg^{-1} in terms of the SWCNT/SnO electrode in the asymmetric device (note the MXene was in excess). The energy density at 1 A g^{-1} was 24.39 Wh kg^{-1} for the SWCNT/SnO electrode in the asymmetric device dropping to 6.66 Wh kg^{-1} at 10 A g^{-1}. The energy density was calculated from the GCD curve using Eq. (8) which considers the non-perfect triangular GCD curve of the device, where t_2 is the time the discharge finished and t_1 is the time after the initial IR drop [55].

$$E = \int_{t1}^{t2} IV_{(t)}dt \tag{8}$$

(Note if accounting for the excess mass of MXene the full results for the device are: 15 kW kg^{-1},9.5 Wh kg^{-1} and 2.6 Wh kg^{-1}).

Cycling data at 10 A g^{-1} shows the enhanced stability obtainable through the small addition of SnO to the SWCNTs with the three-electrode configuration retaining 95% of the initial capacity after 7,500 cycles whilst the asymmetric device retains 90% of its initial capacity.

4. Conclusions

In conclusion, pure SWCNT and SWCNT/SnO inks were successfully manufactured into functioning supercapacitor electrodes. The presence of SnO, although not adding to the capacitance of the electrode in the voltage window, importantly inhibited the oxidation and subsequent degradation of the SWCNT as confirmed by Raman spectroscopy, FTIR, and XPS. We believe that the mechanism for shielding the SWCNTs involves a pseudo-reversible reaction between the sulphate ions and SnO, which leads to the existence of both SnO and Sn_3O_4 after cycling in devices. This led to enhanced cycling stability for electrodes containing a small fraction of SnO with a capacitance of 102 F g^{-1} at 2 A g^{-1} and capacity retention in excess of 95% after 7,500 cycles at 10 A g^{-1}, thus demonstrating the advantage of inhibiting the functionalisation of SWCNTs. The asymmetric device assembled allowed the voltage window to be expanded to 1.8 V using MXene as the negative electrode, with an energy of 24.39 Wh kg^{-1} at 1 A g^{-1} and capacity retention of 90% after 7,500 cycles. Through further optimisation of this device and printing more intricate geometries, we believe this figure can be improved upon.

CRediT authorship contribution statement

Seán Ryan: Conceptualization, Methodology, Formal analysis, Investigation, Writing – original draft, Writing – review & editing, Visualization. **Michelle P. Browne:** Formal analysis, Writing – original draft, Writing – review & editing, Visualization. **Ainur Zhussupbekova:** Investigation, Formal analysis, Writing – review & editing. **Dahnan Spurling:** Methodology. **Lorcan McKeown:** Software, Methodology. **Danielle Douglas-Henry:** Investigation. **Lucy Prendeville:** Investigation. **Sebastien Vaesen:** Investigation. **Wolfgang Schmitt:** Resources. **Igor Shvets:** Resources. **Valeria Nicolosi:** Conceptualization, Resources, Writing – original draft, Writing – review & editing, Supervision, Funding acquisition.

Declaration of Competing Interest

The authors declare that they have no known competing financial interests or personal relationships that could have appeared to influence the work reported in this paper.

Data availability

Data will be made available on request.

Acknowledgments

This study was supported by the European Research Council grant [ERC 3D2DPrint, GA 681544] funded by the European Union. This publication has emanated from research supported in part by a grant from Science Foundation Ireland under Grant number [12/RC/2278_P2]. The authors acknowledge the Advanced Microscopy Laboratory for the provision of their facilities. Microscopy characterization and analysis has been performed at the CRANN Advanced Microscopy Laboratory (AML) (www.tcd.ie/crann/aml/). Seán Ryan wishes to thank the Irish Research Council (GOIPG/2019/2428) for funding a PhD studentship. Michelle P. Browne would like to acknowledge the European Union's Horizon 2020 research and innovation programme under the Marie Skłodowska-Curie grant agreement No. 884318 (TriCat4Energy). Ainur Zhussupbekova would like to acknowledge the funding from Irish Research Council through GOIPD/2022/443 award. For the purpose of Open Access, the author has applied a CC BY public copyright licence to any Author Accepted Manuscript version arising from this submission.

Supplementary materials

Supplementary material associated with this article can be found, in the online version, at doi:10.1016/j.electacta.2023.142168.

References

[1] S. Iijima, Helical microtubules of graphitic carbon, Nature 354 (1991) 56.
[2] B. Earp, et al., Enhancement of electrical conductivity of carbon nanotube sheets through copper addition using reduction expansion synthesis, Mater. Res. Bull. 131 (2020), 110969.
[3] S. Hong, S. Myung, Nanotube electronics: a flexible approach to mobility, Nat. Nanotechnol. 2 (2007) 207–208.
[4] X. Zhou, J.-Y. Park, S. Huang, J. Liu, P.L. McEuen, Band structure, phonon scattering, and the performance limit of single-walled carbon nanotube transistors, Phys. Rev. Lett. 95 (2005), 146805.
[5] R.H. Baughman, A.A. Zakhidov, W.A. de Heer, Carbon nanotubes–the route toward applications, Science 297 (2002) 787–792.
[6] M.-.F. Yu, B.S. Files, S. Arepalli, R.S Ruoff, Tensile loading of ropes of single wall carbon nanotubes and their mechanical properties, Phys. Rev. Lett. 84 (2000) 5552–5555.
[7] Pan, H., Li, J., Yuan, & Feng, P. Carbon Nanotubes for Supercapacitor. doi:10.1007/s11671-009-9508-2.
[8] X. Xiao, et al., Freestanding functionalized carbon nanotube-based electrode for solid-state asymmetric supercapacitors, Nano Energy 6 (2014) 1–9.
[9] B. Pal, S. Yang, S. Ramesh, V. Thangadurai, R. Jose, Electrolyte selection for supercapacitive devices: a critical review, Nanoscale Adv. 1 (2019) 3807–3835.
[10] G.U. Sumanasekera, et al., Electrochemical oxidation of single wall carbon nanotube bundles in sulfuric acid, J. Phys. Chem. B 103 (1999) 4292–4297.
[11] S. Lefrant, et al., SERS spectroscopy studies on the electrochemical oxidation of single-walled carbon nanotubes in sulfuric acid solutions, Synth. Met. 144 (2004) 133–142.
[12] P. Corio, et al., Potential dependent surface Raman spectroscopy of single wall carbon nanotube films on platinum electrodes, Chem. Phys. Lett. 370 (2003) 675–682.
[13] C.M. Campo, J.E. Rodríguez, A.E. Ramírez, Thermal behaviour of romarchite phase SnO in different atmospheres: a hypothesis about the phase transformation, Heliyon 2 (2016) e00112–e00112.
[14] C.-.T. Hsieh, W.-.Y. Lee, C.-.E. Lee, H Teng, Electrochemical capacitors fabricated with tin oxide/graphene oxide nanocomposites, J. Phys. Chem. C 118 (2014) 15146–15153.
[15] K.K. Liu, et al., Flexible solid-state supercapacitor based on tin oxide/reduced graphene oxide/bacterial nanocellulose, RSC Adv 8 (2018) 31296–31302.
[16] V. Velmurugan, U. Srinivasarao, R. Ramachandran, M. Saranya, A.N. Grace, Synthesis of tin oxide/graphene (SnO2/G) nanocomposite and its electrochemical properties for supercapacitor applications, Mater. Res. Bull. 84 (2016) 145–151.
[17] Q. Wang, Y. Tian, S. Guan, Z. Peng, X Fu, Alloying enhanced supercapacitor performance based on oxygen-deficient tin oxide nanorod array electrodes, ACS Appl. Energy Mater. 3 (2020) 11333–11342.
[18] Y. Tian, Q. Wang, Z. Peng, S. Guan, X. Fu, Ni foam-supported tin oxide nanowall array: an integrated supercapacitor anode, Molecules 26 (2021).
[19] A. Murugan, et al., Structural and charge density distribution studies on Tin Oxide nanoparticles for Supercapacitor application, J. Energy Storage 28 (2020), 101194.

[20] M. Borghetti, M. Serpelloni, E. Sardini, D. Spurling, V. Nicolosi, Temperature influence on Ti3C2Tx lines printed by aerosol jet printing, Sens. Actuators A 332 (2021), 113185.
[21] Thommes, M. et al. Physisorption of gases, with special reference to the evaluation of surface area and pore size distribution (IUPAC Technical Report). 87, 1051–1069 (2015).
[22] M.S. Dresselhaus, G. Dresselhaus, R. Saito, A Jorio, Raman spectroscopy of carbon nanotubes, Phys. Rep. 409 (2005) 47–99.
[23] B. Martínez-Sánchez, J. Quílez-Bermejo, E. San-Fabián, D. Cazorla-Amorós, E. Morallón, On the mechanism of electrochemical functionalization of carbon nanotubes with different structures with aminophenylphosphonic acid isomers: an experimental and computational approach, J. Mater. Chem. A 10 (2022) 7271–7290.
[24] Botti, S. Surface-Enhanced Raman Spectroscopy Characterization of Pristine and Functionalized Carbon Nanotubes and Graphene. in (ed. RufoloniA.) Ch. 10 (IntechOpen, 2018). doi:10.5772/intechopen.74065.
[25] O.A. Gurova, et al., Purification of single-walled carbon nanotubes using acid treatment and magnetic separation, Phys. status solidi 256 (2019), 1800742.
[26] M.P. Browne, F. Novotny, M. Pumera, 3D Printed Graphene Electrodes' Electrochemical Activation (2018), https://doi.org/10.1021/acsami.8b14701.
[27] B.R.C. De Menezes, et al., Effects of octadecylamine functionalization of carbon nanotubes on dispersion, polarity, and mechanical properties of CNT/HDPE nanocomposites, J. Mater. Sci. 53 (2018) 14311–14327.
[28] S.-.M. Yuen, C.-C.M. Ma, Y.-.Y. Lin, H.-.C. Kuan, Preparation, morphology and properties of acid and amine modified multiwalled carbon nanotube/polyimide composite, Compos. Sci. Technol. 67 (2007) 2564–2573.
[29] Kim, U.J., Furtado, C.A., Liu, X., Chen, G. & Eklund, P.C. Raman and IR Spectroscopy of Chemically Processed Single-Walled Carbon Nanotubes. (2005) doi:10.1021/ja052951o.
[30] S.K. Mishra, S.N. Tripathi, V. Choudhary, B.D. Gupta, Surface resonance-based fiber optic methane gas sensor utilizing graphene-carbon nanotubes-poly(methyl methacrylate) hybrid nanocomposite, Plasmonics 10 (2015) 1147–1157, https://doi.org/10.1007/s11468-015-9914-5.
[31] J.-.H. Choi, J. Jegal, W.-.N Kim, Fabrication and characterization of multi-walled carbon nanotubes/polymer blend membranes, J. Memb. Sci. 284 (2006) 406–415.
[32] L.S. Cividanes, et al., Cure study of epoxy resin reinforced with multiwalled carbon nanotubes by raman and luminescence spectroscopy, J. Appl. Polym. Sci 127 (2012) 544–553.
[33] G. Kalonga, K. Chinyama, O. Munyati, M. Maaza, Characterization and optimization of P3HT and PCBM blends for photo-absorption, J. Chem. Eng. Mater. Sci. (2013) 93–102, https://doi.org/10.5897/JCEMS2013.0148.
[34] Z. Gao, T.J. Bandosz, Z. Zhao, M. Han, J Qiu, Investigation of factors affecting adsorption of transition metals on oxidized carbon nanotubes, J. Hazard. Mater. 167 (2009) 357–365.
[35] P. Botschwina, The equilibrium geometry and some spectroscopic constants of C5 from large-scale ab initio calculations, J. Chem. Phys. 101 (1994), 234302.
[36] N. Tapia-Ruiz, et al., 2021 roadmap for sodium-ion batteries, J. Phys. Energy 3 (2021) 31503.
[37] C. Fang, et al., Preparation of "natural" diamonds by HPHT annealing of synthetic diamonds, CrystEngComm 20 (2018) 505–511.
[38] A.R. Babar, S.S. Shinde, A.V. Moholkar, K.Y Rajpure, Electrical and dielectric properties of co-precipitated nanocrystalline tin oxide, J. Alloys Compd. 505 (2010) 743–749.
[39] N.M. Shaalan, D. Hamad, A.Y. Abdel-Latief, M.A Abdel-Rahim, Preparation of quantum size of tin oxide: structural and physical characterization, Prog. Nat. Sci. Mater. Int. 26 (2016) 145–151.
[40] W. Zeng, et al., SnO–Sn3O4 heterostructural gas sensor with high response and selectivity to parts-per-billion-level NO2 at low operating temperature, RSC Adv 10 (2020) 29843–29854.
[41] S. Jaśkaniec, et al., Solvent engineered synthesis of layered SnO for high-performance anodes, npj 2D Mater. Appl. 5 (2021) 27.
[42] T.I.T. Okpalugo, P. Papakonstantinou, H. Murphy, J. McLaughlin, N.M.D Brown, High resolution XPS characterization of chemical functionalised MWCNTs and SWCNTs, Carbon 43 (2005) 153–161.
[43] M.T. Martínez, et al., Sensitivity of single wall carbon nanotubes to oxidative processing: structural modification, intercalation and functionalisation, Carbon 41 (2003) 2247–2256.
[44] V.A. Davis, et al., True solutions of single-walled carbon nanotubes for assembly into macroscopic materials, Nat. Nanotechnol. 4 (2009) 830–834.
[45] P. Puech, et al., Charge transfer between carbon nanotubes and sulfuric acid as determined by Raman spectroscopy, Phys. Rev. B 85 (2012), 205412.
[46] A. Metrot, J.E. Fischer, Charge transfer reactions during anodic oxidation of graphite in H2SO4, Synth. Met. 3 (1981) 201–207.
[47] J.O. Besenhard, et al., Anodic oxidation of graphite in H2SO4 dilatometry — in situ X-ray diffraction — impedance spectroscopy, Synth. Met. 7 (1983) 185–192.
[48] H. Pan, J. Li, Y Feng, Carbon nanotubes for supercapacitor, Nanoscale Res. Lett. 5 (2010) 654.
[49] T. Brousse, D. Bélanger, J.W. Long, To be or not to be pseudocapacitive? J. Electrochem. Soc. 162 (2015) A5185.
[50] P. Simon, Y. Gogotsi, B. Dunn, Where do batteries end and supercapacitors begin? Science 343 (2014) 1210–1211.
[51] T.S. Mathis, et al., Energy storage data reporting in perspective—guidelines for interpreting the performance of electrochemical energy storage systems, Adv. Energy Mater. 9 (2019), 1902007.
[52] A. Noori, M.F. El-Kady, M.S. Rahmanifar, R.B. Kaner, M.F. Mousavi, Towards establishing standard performance metrics for batteries, supercapacitors and beyond, Chem. Soc. Rev. 48 (2019) 1272–1341.
[53] R. Díaz, I. Díez-Pérez, P. Gorostiza, F. Sanz, J.R Morante, An electrochemical study of tin oxide thin film in borate buffer solutions, J. Braz. Chem. Soc. 14 (2003) 523–529.
[54] Q. Jiang, N. Kurra, M. Alhabeb, Y. Gogotsi, H.N. Alshareef, All pseudocapacitive MXene-RuO2 asymmetric supercapacitors, Adv. Energy Mater. 8 (2018), 1703043.
[55] Y. Shao, et al., Design and mechanisms of asymmetric supercapacitors, Chem. Rev. 118 (2018) 9233–9280.
[56] L. Guan, L. Yu, G.Z. Chen, Capacitive and non-capacitive faradaic charge storage, Electrochim. Acta 206 (2016) 464–478.
[57] T. Gu, B. Wei, Fast and stable redox reactions of MnO2/CNT hybrid electrodes for dynamically stretchable pseudocapacitors, Nanoscale 7 (2015) 11626–11632.
[58] C. Zhan, et al., Understanding the MXene pseudocapacitance, J. Phys. Chem. Lett. 9 (2018) 1223–1228.